

RESEARCH ARTICLE

10.1002/2017JB015296

Key Points:

- Imaging is by μ CT with pore-scale finite element modeling representing the pore network in synthetic cores for single-phase fluid flow.
- Heterogeneity and anisotropy of the pore systems are proved to have a significant impact on flow fields in the 3-D pore network
- A new equation is established to predict the transition of flow patterns as a function of the apparent permeability and Reynolds number

Correspondence to:

Y. Zhao and G. Zhu,
zhaoyx@cumtb.edu.cn;
guangpeizhu@163.com

Citation:

Zhao, Y., Zhu, G., Zhang, C., Liu, S., Elsworth, D., & Zhang, T. (2018). Pore-scale reconstruction and simulation of non-Darcy flow in synthetic porous rocks. *Journal of Geophysical Research: Solid Earth*, 123, 2770–2786. <https://doi.org/10.1002/2017JB015296>


Received 30 NOV 2017

Accepted 23 MAR 2018

Accepted article online 30 MAR 2018

Published online 16 APR 2018

Pore-Scale Reconstruction and Simulation of Non-Darcy Flow in Synthetic Porous Rocks

Yixin Zhao^{1,2,3} , Guangpei Zhu^{1,3}, Cun Zhang^{1,2,3}, Shimin Liu⁴, Derek Elsworth⁴, and Tong Zhang^{1,3}

¹Beijing Key Laboratory for Precise Mining of Intergrown Energy and Resources, China University of Mining and Technology, Beijing, China, ²State Key Laboratory of Coal Resources and Safe Mining, China University of Mining and Technology, Beijing, China, ³College of Resources and Safety Engineering, China University of Mining and Technology, Beijing, China, ⁴Energy and Mineral Engineering, G³ Center and EMS Energy Institute, Pennsylvania State University, University Park, PA, USA

Abstract We image synthetic porous rocks of varied porosity and pore size by micro-computed tomography with pore-scale finite element modeling representing the pore space for single-phase fluid flow. The simulations quantify the key features of microscale flow behavior in the synthetic cores. The smaller the permeability, the greater the critical pressure gradient required for the onset of non-Darcy fluid flows, and the easier the emergence of nonlinear seepage within the tested cores. The relationship between permeability and porosity from different methods shows a power law correlation with pressure. Structural heterogeneity and anisotropy of the pore systems are shown to have a significant impact on transport through the three-dimensional pore model—exhibiting irregular flow fields. The simulated permeabilities of the tested cores vary by a factor of 2–5 depending on the fluid flow directions. With the increase of flow seepage velocity, the flow regime deviates from Darcy linear relationship and non-Darcy behavior (inertia) leads to a reduction in the effective permeability of the core. Both experiments and modeling demonstrate that the larger the porosity and permeability, the stronger the non-linear phenomenon of the seepage within the pore space. A method is proposed to estimate the non-Darcy coefficient β based on simulation results, which provides a good prediction for all the tested cores. A new equation is established to predict the transition of flow patterns as a function of the apparent permeability K^* and Reynolds number Re . The K^*-Re model provides a theoretical approach to dynamically describe the transition from Darcy to Forchheimer flow.

1. Introduction

The pore structure and macroscopic properties directly influence the fluid flow characteristics of reservoir rock. This is particularly important in unconventional oil and gas resource evaluation, as well as in the exploration and development of CO₂ geological storage and groundwater seepage (Bachu, 2000; Leahy-Dios et al., 2011; Yang et al., 2013)—where flow pathways may be irregular, tortuous, and constricted. Since routine experimental methods may change the pore structure of reservoir rock under stresses, the direct nondestructive scanning technologies may be adopted to define the spatial characteristics of pore structure (Dunsmuir et al., 1991; Spanne et al., 1994). Imaging by micro-computed tomography (μ CT) X-ray tomography is able to establish the three-dimensional pore throat architecture based on real rocks at different length-scales and define the spatial distribution and connectivity of pores and throats (Zhang et al., 2014). Arns and Knackstedt (2004) predicted the permeability of Fontainebleau sandstone based on microtomographic images with the simulation of fluid permeability in close agreement with experiment results. Dong et al. (2007) developed a maximal ball algorithm to extract topologically equivalent pore network models of sandstone and carbonate based on μ CT images and concluded that both the extracted network structures and predicted single- and two-phase transport properties were in good agreement with the benchmark data. Yao et al. (2010) used a quantitative method to estimate the characterization of pore types, producible porosity, pore structure, and spatial disposition of pore-fractures in coals. The aforementioned literatures indicate that μ CT is capable of modeling and spatial visualization of pores and fractures.

Seepage laws may be determined within the connected pore space of rocks by simulating flow directly from reconstructed three-dimensional μ CT images (Ovaysi & Piri, 2010). Sukop et al. (2013) applied the Lattice Boltzmann method to simulate 3-D flows in macroporous limestone to estimate intrinsic permeability from pore structure and to account for inertial flow that leads to a deviation from Darcy's law. Bird et al. (2014)

used the commercial software Avizo and COMSOL to simulate fluid flow in the pore space of a carbonate rock and calculated sample permeability and the electric forming factor. Liu et al. (2014) completed pore-scale numerical simulations of the permeability and elastic parameters of sandstone and validated results against experimental measurements. Ni et al. (2017) quantitatively characterized the porosity distribution in coal and determined the absolute permeability of samples based on μ CT measurements and coal bed methane flow simulation. It is especially important to consider non-Darcy flow behaviors in the near-wellbore region and in propped hydraulic fractures where constricted flows result in strong spatial accelerations. Such nonlinear flow effects are commonly described by the Forchheimer equation, in which the deviation from the Darcy's law is proportional to the non-Darcy coefficient β factor (Newman & Yin, 2013). Several numerical studies of non-Darcy flow behavior have been based on realistic 3-D images of porous rocks. Chukwudozie et al. (2012) used Lattice Boltzmann models to quantitatively predict the absolute permeability and β factor of Castlegate sandstone—the numerical results were in good agreement with experimental measurements. Muljadi et al. (2016) employed a finite-volume method to simulate fluid flows based on 3-D images of a beadpack in Bentheimer sandstone and Estailades carbonate. These models predicted non-Darcy flow parameters such as the β factor, and the onset of non-Darcy flow. Wang et al. (2016) carried out a numerical simulation of gas flow in coal pores and fractures and calculated the permeability and non-Darcy coefficients. Simulation results showed that the gas flowing even at the microscale ($<100 \mu\text{m}$) showed characteristics of Forchheimer behavior. However, few of the numerical studies have addressed and explored the key features and mechanisms of pore characteristics that impact the non-Darcy flow response in a range of real reservoir rocks.

In this work, we quantify and characterize the pore structures of artificial cores and develop an equivalent Pore Network Model. A finite element method is implemented using ANSYS Fluent to simulate fluid flows directly on the 3-D image realizations of three contrasting porous cores with varying complexity and heterogeneity. By completing the flow simulations directly in the pore-scale images of the networks, we examine the key features of the pressure field and velocity field distributions within these samples during the flow transition from Darcy into the non-Darcy flow regime. The results enable a better understanding of the underlying mechanisms of, and the effect of pore characteristics on, the flow transition to non-Darcy flow.

2. Theoretical Background

2.1. Theoretical Background of Non-Darcy Flow

At flow rates above a critical stagnant pressure gradient, the pressure drop is linearly proportional to the flow rate and is described by the Darcy equation (Darcy, 1912):

$$-\frac{dp}{dx} = \frac{\mu v}{K_D} \quad (1)$$

where x represents the direction of flow, p is the pressure, v is the velocity, μ is the dynamic fluid viscosity, and K_D is Darcy permeability.

As the flow rates increase, the Darcy's law no longer holds; the relationship between pressure gradient and velocity becomes nonlinear due to inertial effects and behavior may be described by the Forchheimer equation (Forchheimer, 1901):

$$-\frac{dp}{dx} = \frac{\mu v}{K_F} + \rho \beta v^2 \quad (2)$$

where ρ is the fluid density and K_F is the Forchheimer permeability which is close to but not equal to K_D , and β is the non-Darcy coefficient of porous medium.

2.2. Criterion for Non-Darcy Flow and the β Factor

In non-Darcy flow the pressure drop is caused by a combination of viscous (linear term) and inertial forces (non-linear term). In this paper, the criterion for non-Darcy flow is the threshold when the pressure drop due to the linear term becomes less than 99% of the total (Comiti et al., 2000).

Table 1
Petrophysical Properties of the Artificial Cores

Sample no.	Diameter (mm)	Length (mm)	Porosity (%)	Permeability (μm^2)
S1	24.79	50.99	38	4.59
S2	24.78	50.96	42	10.19
S3	23.29	50.56	49	20.38

K^* , defined as the dimensionless apparent permeability, is the ratio of the pressure drop of the Darcian component to the non-Darcian component. This reflects the extent to which the non-Darcy component deviates from linear Darcy flow. K^* is mathematically defined as

$$K^* = \frac{\frac{\mu}{K_D} v}{\frac{\mu}{K_F} v + \rho \beta v^2} \quad (3a)$$

$$K^* = \frac{K_{app}}{K_D} \quad (3b)$$

To further demonstrate the deviation from Darcy to non-Darcy flow, the apparent permeability K_{app} is defined as

$$\frac{1}{K_{app}} = \frac{1}{K_F} + \beta \frac{\rho v}{\mu} \quad (4)$$

According to the earlier definition of non-Darcy flow, the end of the Darcy flow regime is the point when $K^* = 0.99$. In addition, the inverse of the apparent permeability $\frac{1}{K_{app}}$ is plotted as a function of $\frac{\rho v}{\mu}$ based on equation (4). Then the non-Darcy coefficient β can be calculated from the slope of the function (Muljadi et al., 2016).

In a porous medium, the Reynolds number (Re) is not intuitively related to the flow, but where non-Darcian flow is important, Re is defined as

$$Re = \frac{\rho v L_0}{\mu} \quad (5)$$

where v is the average volumetric velocity and L_0 is the grain diameter estimated through CT imaging.

2.3. The K^* - Re Model for the Transition From Darcian to Non-Darcian Flow Regimes

Non-Darcian flow behavior emerges from the laminar flow regime at relatively high Re as the inertial force dominates over viscous forces as the flow rate increases (Bear, 1972; Chaudhary et al., 2011). For flows, the transition from Darcy to non-Darcy regimes is a dynamic evolution depending on the flow rate intensity for a given pore structure. To account for this transition, a dimensionless model as shown is proposed to describe the transition from viscous to inertial flows in a porous medium. The velocity v is replaced by the Re , and the K^* - Re relationship as

$$K^* = \frac{1}{1 + \alpha \beta \frac{K_D}{L_0} Re} \left(\alpha = 1, \quad Re < 1 \sim 10; \text{ and } \alpha \neq 1, \quad Re > 1 \sim 10 \right) \quad (6)$$

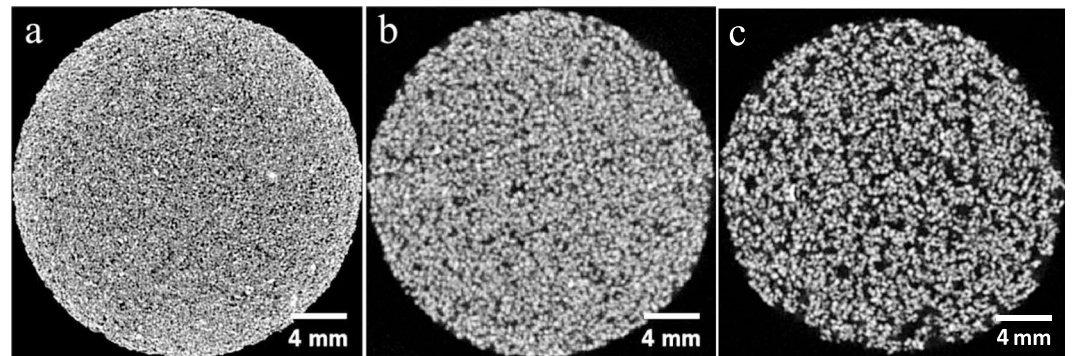


Figure 1. Typical 2-D slices of the tested artificial cores obtained by micro-CT. In the slices, the luminous regions represent rock skeleton and dark regions indicate pores. (a) sample S1, (b) sample S2, and (c) sample S3.

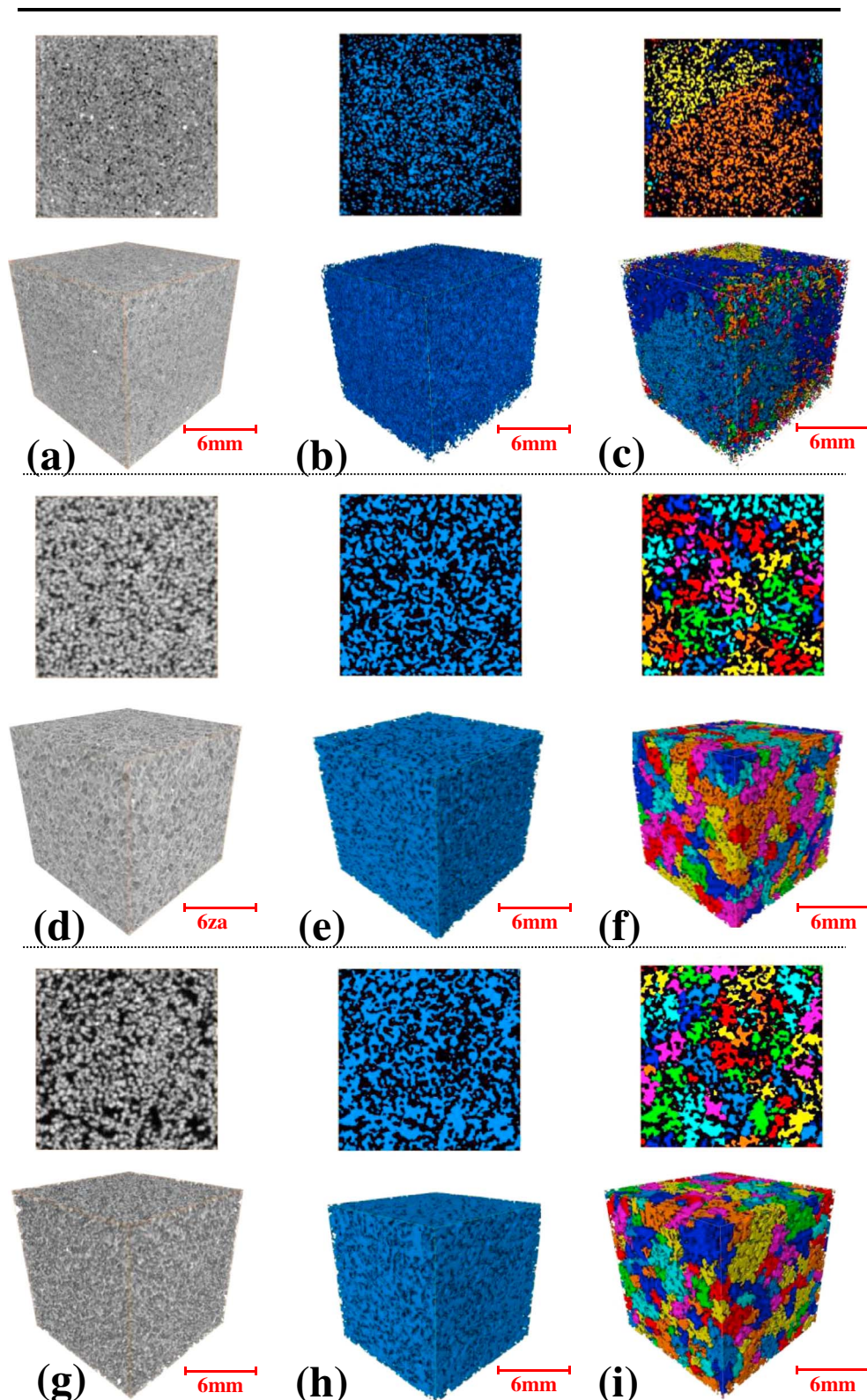


Figure 2. 2-D and 3-D reconstructions of VOIs in the (a–c) samples S1, (d–f) S2, and (g–i) S3. In the first column, the upper parts represent the regions of interest in the CT slices and the below parts are the volume of interest (VOI) of $300 \times 300 \times 300$ voxels in the artificial core samples. The second column shows 2-D and 3-D representations of the pore structures after segmentation (blue represents pores). The last column shows the generated label field to explore the 2-D and 3-D structures of micropores based on segmentation images. The individual pores are colored differently at random in figures (c), (f), and (i).

Table 2
Properties of Pore Structure Extracted From Reconstructed Model of Artificial Core Samples Based on CT Images

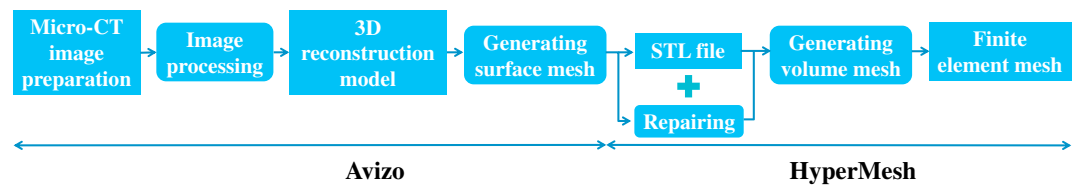
Sample no.	Experimental porosity Φ_m	Calculated porosity Φ_c	Ave. pore radius $r/\mu\text{m}$	Ave. throat radius $r_t/\mu\text{m}$	Ave. pore volume $V/\times 10^8 \mu\text{m}^3$	Specific surface area S_p (1/cm)	Tortuosity τ	Grain diameter $L_0/\mu\text{m}$
S1	0.38	0.37	235	132	1.72	1368	1.37	1042
S2	0.42	0.41	378	134	3.13	1065	1.29	842
S3	0.49	0.48	393	158	4.55	877	1.27	708

where coefficient α is the corrected coefficient for inertial effects in non-Darcy flow regimes. The Darcy permeability K_D is approximately equal to the Forchheimer permeability K_F and corrected coefficient $\alpha = 1$ at the low flow rate ($Re < 1-10$). The ratio of Darcy permeability K_D to Forchheimer permeability K_F is not equal to unity, and the inertial effects cannot be ignored for high-velocity flow ($Re > 1-10$). Thus, a coefficient α (not equal to 1) is added to correct Re for nonnegligible inertial effects.

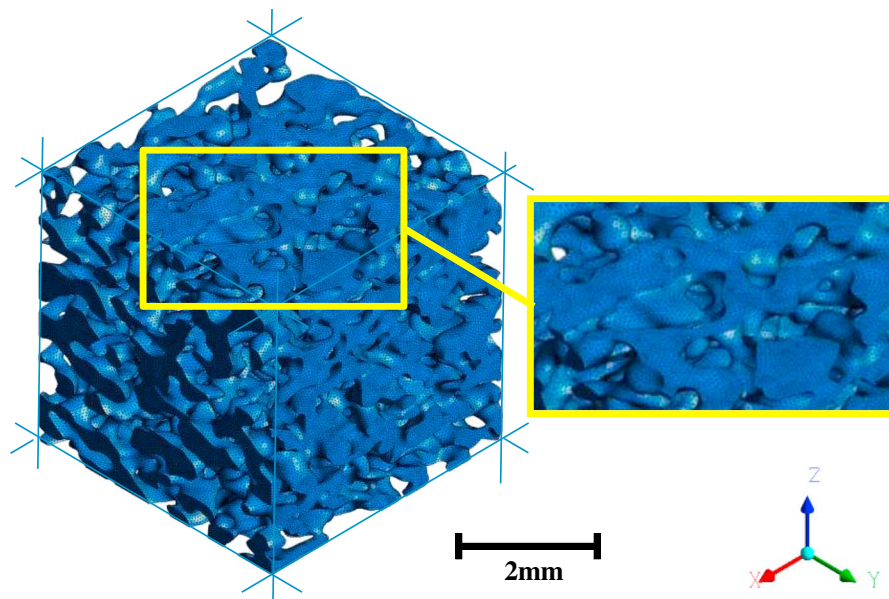
3. Material and Methods Core-Scale Pore Structure Reconstructions and its Validation

3.1. Core Sample Preparation and CT Imaging

Laboratory experiments are critical in the study of fluid flow through porous rocks. In this study, we use synthetic cores as control as these offer reproducible (unlike natural cores) characteristics even in destructive



(a)



(b)

Figure 3. Work flow and result of finite element mesh model generating. (a) Work flow of mesh model generating. (b) Finite element mesh model of pore spaces of sample S2 through which the flows are simulated directly. The samples have the dimensions of $5 \times 5 \times 5 \text{ mm}^3$.

Table 3
Properties of Mesh Models of the Artificial Cores

Sample no.	Size		Mesh		Effective porosity
	Number of voxels	Dimensions/mm ³	Tetrahedra × 10 ⁶	Nodes × 10 ³	Φ _e /%
S1	100 × 100 × 100	5 × 5 × 5	1.8	418	28
S2			1.9	438	37
S3			2.0	459	47

experiments (Pi, 2010). The three artificial cores (HRXC Core Company, China) comprise cementation of quartzite and colophony. In this study, we choose to use the artificial core for the study because two main reasons. The first reason is that the artificial core can be synergized in such a way that the physical property of rock are as desired. The second reason is that the artificial core can physical mimic the real reservoir rock properties and the numerical model construction is more reliable and reproducible. The petrophysical properties of the artificial cores are listed in Table 1. The permeability is measured using the transient gas method, and the porosity of the artificial cores is measured by nuclear magnetic resonance (NMR) (Xu et al., 2015; Zhao et al., 2017). The permeability results were provided by Core Company, and the porosities of artificial cores are calculated directly using the integral area of the NMR T_2 spectrum.

With the cores assembled, CT is used to recharacterize the pore structure and to reconstruct the pore space for the fluid flow simulation. All the imaging is performed using an ACTIS-225FFI μ CT scanner manufactured by BIR Corporation in USA. The X-ray source is a 225 kV Feinfocus focal spot, which allows for highest resolution down to 5 μ m for an object of 8 mm. The experimental sample is a 25-mm diameter and 50-mm length cylindrical sample. Samples were dried before scanning, and the scanner operated at 180 kV and 200 μ A. The computed microtomography scans were acquired at \sim 50- μ m voxel size. Figure 1 shows the typical 2-D images of the artificial cores obtained by CT.

The pore structure, together with the solid grains, are reconstructed and analyzed by commercial 3-D image processing and analysis software Avizo (FEI Co., USA). A volume of interest (VOI) of 300 × 300 × 300 voxels in the artificial core samples is selected for further analysis of the porosity, the tortuosity, the pore size, and the grain diameter. Here the 3-D volumetric porosity of the VOI was estimated by using the Avizo quantification module.

The tortuosity of pores was calculated using the Avizo *Centroid Path Tortuosity* module (Thermo Fisher Scientific & FEI, 2013). The Otsu method (Boone et al., 2014; Keller et al., 2011; Korvin, 2016; Otsu, 2007; Zhang et al., 2015), an automated threshold segmentation method in the Avizo *Auto Thresholding* module, was used to obtain the relationship between threshold and calculated porosity. By comparing the inversely estimated porosity with the measured porosity through NMR experiments, the optimal thresholds were selected to segment the pore volume in the VOIs of the artificial cores. Then the segmented pore volumes were further processed by the Avizo *Separate Objects* algorithm to generate a *Label Field*. The pore and throat radii are measured by quantitative analysis of the separated *Label Field* using the Avizo *Label Analysis* and *Generate Pore Network Model* module (Thermo Fisher Scientific & FEI, 2013), respectively. Similarly, the grain diameter is measured based on the separated grain volume using the Avizo *Label Analysis*.

Figure 2 shows the 2-D and 3-D reconstructions of VOIs in the artificial core samples. The pore structure properties of cores extracted from the reconstructed model are listed in Table 2.

3.2. Meshing and Numerical Modeling

To investigate fluid flow through realistic pore geometry of the porous medium, the 3-D reconstructed model has to be transformed into an appropriate finite element mesh. Following previous studies (Bird

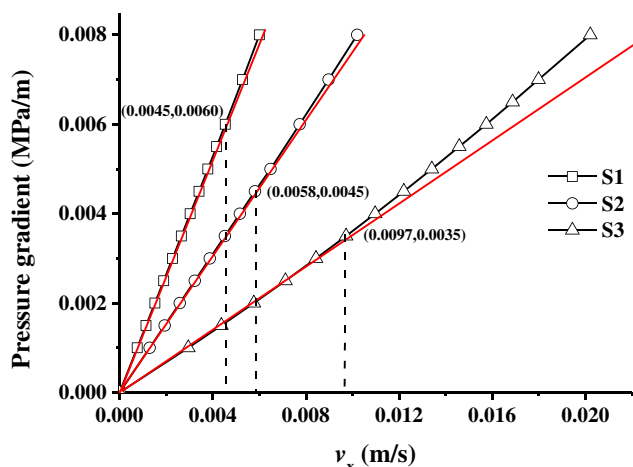


Figure 4. Results of pressure gradients for sample S1, S2, and S3 as they deviate from the linear relationship with the increasing velocities. The symbols of samples represent the simulated pressure gradient, and the red lines represent the assumed pressure gradients which obey Darcy's law. The black dashed lines represent the onset of the Forchheimer flow regimes. The point coordinates indicate the critical pressure gradient and critical Reynolds number for the sample S1, S2, and S3, respectively, which depict the onsets of non-Darcy flow.

Table 4
Comparison of the Permeability Results Based From Different Models

Sample no.	Flow direction	Permeability $K/\mu\text{m}^2$			
		Darcy's law	Average values of Darcy's law	Kozeny-Carman equation	Experiment
S1	X	7.58	4.62	5.27	4.59
	Y	4.76			
	Z	1.52			
S2	X	12.91	9.91	10.86	10.19
	Y	11.59			
	Z	5.28			
S3	X	26.53	26.26	18.85	20.38
	Y	32.97			
	Z	19.28			

et al., 2014; Song et al., 2017; Yan et al., 2010), we use HyperMesh to transform CT images into a suitable finite element. The work flow of numerical meshing is shown in Figure 3a.

Once the 3-D reconstructed model is selected, it was saved as a surface and generates a STereoLithography file that represented the pore surface by the built-in Avizo Fire surface editor (Bird et al., 2014). The isosurface extraction from a 3-D binary image is accomplished using a marching cubes algorithm (Lorenson & Cline, 1987). However, this algorithm is of limited applicability since it produces inconsistent nonmanifold surfaces, as well as surfaces with an excessive number of triangles (Yan et al., 2010). To address this challenge, the software HyperMesh was used to repair the surfaces and improve the isosurface quality with this repaired isosurface processed to generate volumetric meshes, which could be imported into the finite element simulators.

The selection of representative subsamples and the determination of the size of the subsamples are very important and may be improved through optimization (Bear, 1972). By comprehensively considering the representative size of the samples and the quality of the meshes, it was found that the representative size of the sample with $100 \times 100 \times 100$ voxels was sufficient to provide the consistency and generality in our previous studies (Zhao et al., 2017). Thus, this sample size was chosen in the study to analyze the fluid flow properties. It should be noted that the effective porosity Φ_e of the finite element mesh model is less than the experimentally measured porosity Φ_m and the calculated porosity Φ_c from the Avizo software (Table 3). This difference is possibly attributed to the fact that only the interconnected pores are taken into account for the seepage channels in the mesh model (Gruber et al., 2012). Figure 3b illustrates that the application of the mesh modeling method in the simulation of the artificial core samples. The samples have a dimension of $5 \times 5 \times 5 \text{ mm}^3$, and the detailed information is listed in Table 3.

Finite element simulations using ANSYS Fluent recover steady incompressible flow models through the pore space of a porous medium accommodating the Navier-Stokes and continuity equations as

$$\begin{aligned} \nabla p &= \mu \nabla^2 \mathbf{v} - \rho(\mathbf{v} \cdot \nabla) \mathbf{v} \\ \nabla \cdot \mathbf{v} &= 0 \end{aligned} \quad (7)$$

In the simulations, standard fluid properties for water are used: $\rho = 1,000 \text{ kg/m}^3$ and $\mu = 0.001 \text{ Pa s}$. A constant pressure boundary condition at the inlet and the outlet is applied. No-slip boundary conditions are assigned to the pore-grain interface, as well as to the domain boundaries parallel to the flow direction (Yan et al., 2010).

4. Numerical Description of Microscale Flow Behavior in Porous Media

In Figure 4, the pressure gradients are plotted as a function of volumetric velocities showing the onset of non-Darcy flow behavior as fluid velocity increases (Muljadi et al., 2016). The Re corresponding to the critical value of Darcy flow and non-Darcy flow of samples S1, S2, and S3 are 4.69, 4.88, and 6.87 m/s, respectively. The smaller the permeability of artificial core, the greater the critical pressure gradient for the transition to non-Darcy flow, and the lower the critical Re , which indicates that the transition to non-Darcy flow is more

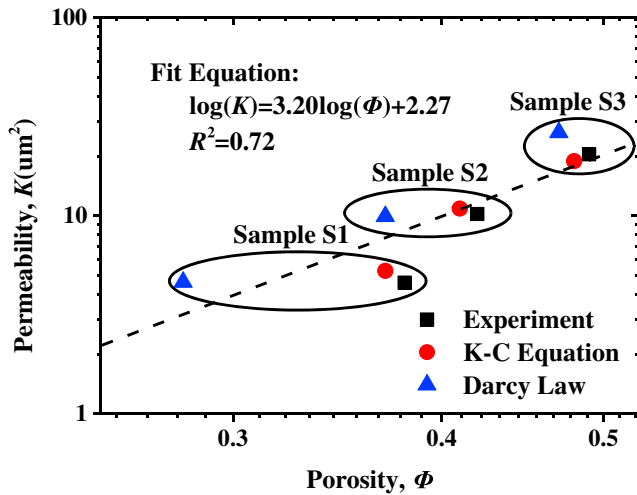


Figure 5. The distribution of the permeability versus porosity from different methods on log-log axes. Different methods are represented by different colors and symbols. The dashed line represents fit line for $K = A\Phi^B$, where constant $A = 10^{2.27}$ and power law exponent $B = 3.20$.

easily to occur. The emergence of nonlinear seepage phenomena coincides with a decrease of porosity and an increase of tortuosity; for S1 we have the sample with lowest critical Re corresponding to the lowest porosity and the largest tortuosity, see Table 2.

4.1. Darcy Permeability and Model Comparison

When the flow rate is proportional to the pressure drop, the permeability of the sample may be calculated using Darcy's law as

$$K_D = \frac{Q\mu L}{A\Delta p} \quad (8)$$

where A is the sample cross-sectional area perpendicular to the flow, L is the sample length, and Q is the flow rate.

At low flow rates, that is, $K^* = 0.99$, the Darcy permeabilities in three orthogonal directions are calculated and listed in Table 4. The Kozeny-Carman permeability based on the properties of pores can be estimated using the Kozeny-Carman equation as

$$K_{K-C} = \frac{\Phi_c}{2\tau^2 S_p^2} \times 10^8 \quad (9)$$

where Φ_c is the porosity of the mesh models and τ is the tortuosity. S_p in cm^{-1} is the specific surface based on pore volume measured from the CT images. K_{K-C} in m is the Kozeny-Carman permeability. Table 4 shows that the calculated Darcy permeability K_D is different in each direction, illustrating that the tested cores are anisotropic and may vary by a factor of 2–5. As shown in Figure 5, there are very good agreements between the experimental permeability data and the prediction of equations (8) and (9). The predicted permeability K_{K-C} is close to the measured permeability, indicating that bundle of capillary tube model is suitable in representing artificial cores of high porosity. The relationship between permeabilities and porosities is in the form of a power law for the tested artificial cores (Schaap & Lebron, 2001). It should be noted that the effective porosity Φ_e is less than the experimentally derived porosity, but the permeability based on Darcy's law is similar to experimental measurements. The results demonstrate that only interconnected pores contribute to the fluid flow (Ahuja, 1989).

4.2. The Characteristics of Non-Darcy Flow Within Pore Channel

Figure 6 shows the results for fluid pressure and velocity distributions within bulk pore volume of sample S1 along a single-channel in the X , Y , and Z directions. As shown in Figure 6, the pressure decreases gradually along the fluid flow direction and the maximum pressure drop occurs in narrow pore throats near the inlet. In the seepage field images, the flow velocity increases rapidly when the pore channel is narrow. This rapid change in seepage velocity is reflected by the clear change in rendered color on the seepage field images, with the change of the seepage velocity relatively slow in the large pore channels. Moreover, the flow path does not cover the entire pore space because of the complex pore geometry, which hinders the fluid flow (Ni et al., 2017).

In order to analyze the pore-scale seepage characteristics along different directions for single-phase flow, the cross sections at different positions along the axis direction (i.e., X , Y , and $Z = 0.05, 1.0, 1.5, 2.0, 2.5, 3.0, 3.5, 4.0, 4.5$, and 5.0 mm, in which X , Y , and Z indicate the distances from the inlet section) are selected, and the results for velocity distributions of different sections under the same pressure gradient are calculated as shown in Figure 7.

Figure 7a shows that the average areal velocities of each sample have different values at different cross sections along the flow directions. Due to the heterogeneity of the cores, the changes in flow velocities along different flow pathways are irregular. As shown in Figure 7b, the average seepage velocities within the bulk pores follow the sequence of $S3 > S2 > S1$. Based on the analysis of pore microstructure, this is attributed to the larger pore channels in the high-porosity cores providing less viscous resistance to the fluid flow.

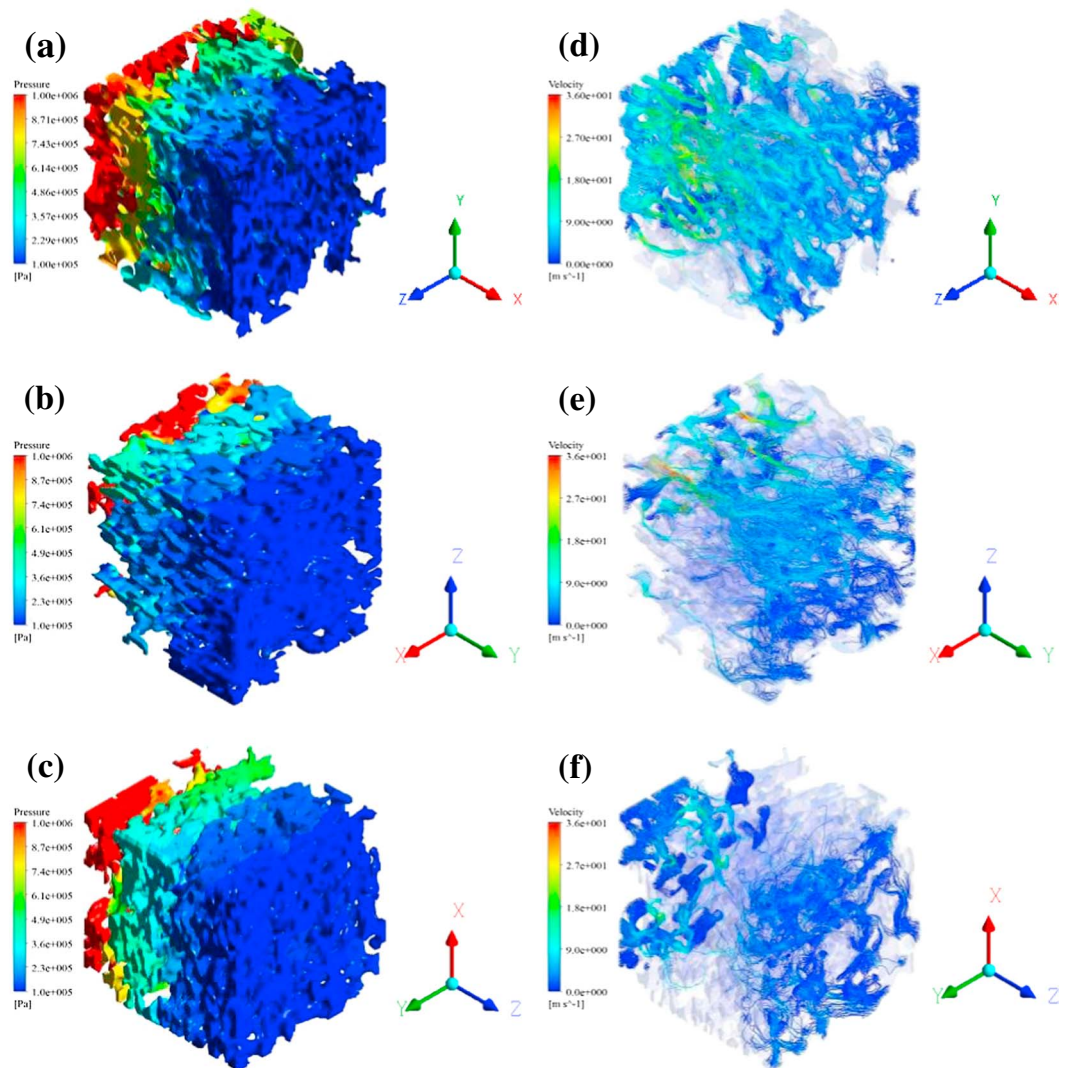


Figure 6. Results for the velocity distributions of artificial core samples at different cross-sections. (a) Average area velocity V of samples along the flow directions. (b) The curves of average velocity V_{avg} versus flow length in the artificial core samples, where V is the average area velocity extracted from cross sections along the flow directions, and V_x , V_y , and V_z represent average area velocities in X , Y , and Z directions, respectively. Average velocity V_{avg} is calculated from the average area velocity V_x , V_y , and V_z , that is, $V_{\text{avg}} = \sqrt{V_x^2 + V_y^2 + V_z^2}/3$.

4.3. Flow Patterns of Non-Darcy Flow Transition and Analyses

The results suggest a small permeability deviation in the different flow directions (varying by a factor of 2–5) and no clear dependence of the magnitude of the permeability on direction (Sukop et al., 2013). For the sake of simplicity, the flow simulation is only carried out in the X direction. To better depict the transition from Darcy to Forchheimer flow regimes, the dimensionless permeability K^* for three samples are calculated as functions of Re , as shown in Figure 8. The flow regimes span Re from 0 to 5,000 and are divided into three zones based on the rate of change of permeability K^* . Zone I represents Darcy flow, and the other two zones demonstrate Forchheimer flows (Bear, 1972; Chaudhary et al., 2011). The functional model for K^*-Re describes the proportion of the pressure loss caused by the Darcy term to total pressure loss (Xu et al., 2012). For the same porous medium, the dimensionless permeability K^* gradually decreases with an increase in the Re , reflecting that the nonlinear component dominates over the linear term in the Forchheimer regime (high flow rates).

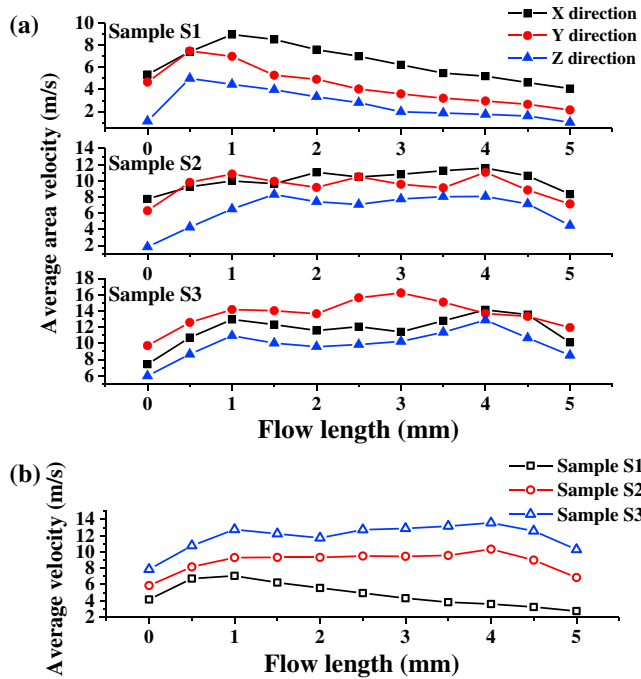


Figure 7. (a) The distribution of volumetric velocities of sample S1 in three directions with applied pressure gradients. (b) The relationship between pressure gradient of sample S1 and velocity ratio in different directions.

2011). Thus, for the chosen artificial cores of high porosity (effective porosity $\geq 28\%$) in this paper, the larger the pore space in the core sample, and the less the limitation of the pore boundaries to the flow of fluid, the easier the development of nonlinear phenomena and the establishment of non-Darcian flow regimes.

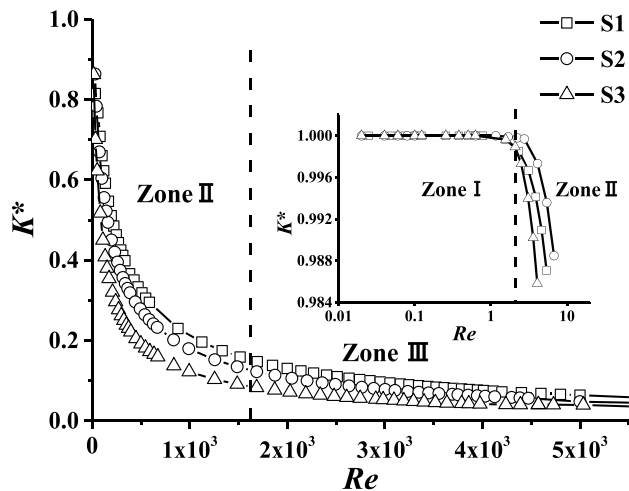


Figure 8. Curves of dimensionless permeability K^* versus Re depicting the transition from Darcy to Forchheimer flow regimes for samples S1, S2 and S3. The regime is Darcy flow in the zone I, that is, $Re < 1-10$ (Bear, 1972). When $10 < Re < 1,600$, the regime in the zone II becomes non-Darcy flow and the permeability K^* decreases sharp due to a fast initial growth of eddies. The flow enters zone III when $Re > 1,600$, and the asymptote in K^* is due to the slowing growth of eddies (Chaudhary et al., 2011).

With the growth of the flow velocity, the flow regime deviates from Darcy (linear) relationship and this non-Darcy behavior leads to a reduction in the effective permeability. This only occurs when the applied pressure gradient is large enough to achieve nonlinear flow (Sukop et al., 2013). The reduction in the permeability is due to the effective narrowing of the flow channels as a consequence of the growth in recirculating eddies that partially fill the void space (Chaudhary et al., 2011; Fourar et al., 2004). This is apparent from the flow patterns in the porous medium for different flow velocities. Figure 9 shows the streamlines within the pore space of sample S1 at $Re = 20$, $Re = 600$, and $Re = 2,200$. As the Re increases, steady state eddies emerge in the pore spaces and reduce the effective dimension of the void that accommodates the flow. This reduction is physically reflected by the reduction in apparent permeability in the high-velocity regime.

The effects of geometry of pore structure on flow transition are identified from the tested samples within an effective porosity range of 0.28–0.47, as shown in Figure 8. At a given Re within the non-Darcy flow regime, it is observed that the relationship between the K^* factors of different samples is $K^*(S1) > K^*(S2) > K^*(S3)$. This indicates that the K^* factor decreases with increasing porosity of the synthetic core. This demonstrates that the larger the porosity of the artificial core samples, the more obvious the nonlinear phenomenon of the seepage within the pore space (Thauvin & Mohanty, 1998). For high-velocity non-Darcy flow, the numerical results show that there is a faster growth of eddies in the broad channels than in the narrow channels (Chaudhary et al.,

2011). Thus, for the chosen artificial cores of high porosity (effective porosity $\geq 28\%$) in this paper, the larger the pore space in the core sample, and the less the limitation of the pore boundaries to the flow of fluid, the easier the development of nonlinear phenomena and the establishment of non-Darcian flow regimes.

$$K^* = \frac{1}{1 + Bv}, \quad B = \frac{\rho K_D}{\mu} \beta \quad (10a)$$

At low flow rates, $Re < 1-10$, the Darcy permeability K_D is approximately equal to the Forchheimer permeability K_F ; thus, equation (3a) is formulated as

$$K^* = \frac{1}{\frac{K_D}{K_F} + Bv} \quad (10b)$$

At high flow rates, the coefficient B is determined only by the non-Darcy coefficient β for a given medium and fluid (Thauvin & Mohanty, 1998; Xu et al., 2012), and K^* is significantly affected by pore structure; when the flow enters the Forchheimer flow regime, the permeability K^* is determined by β and K_F , and K^* is affected not only by pore structure but also by other inertial factors such as currents in eddies. These results can be explained via the evolution of interstitial flow patterns within the pores for different seepage velocities (Muljadi et al., 2016). Figure 10a shows that the flow in the Darcy regime ($Re = 1$) permeates the entire pore space and the resulting pathways are more tortuous. Darcy flow is

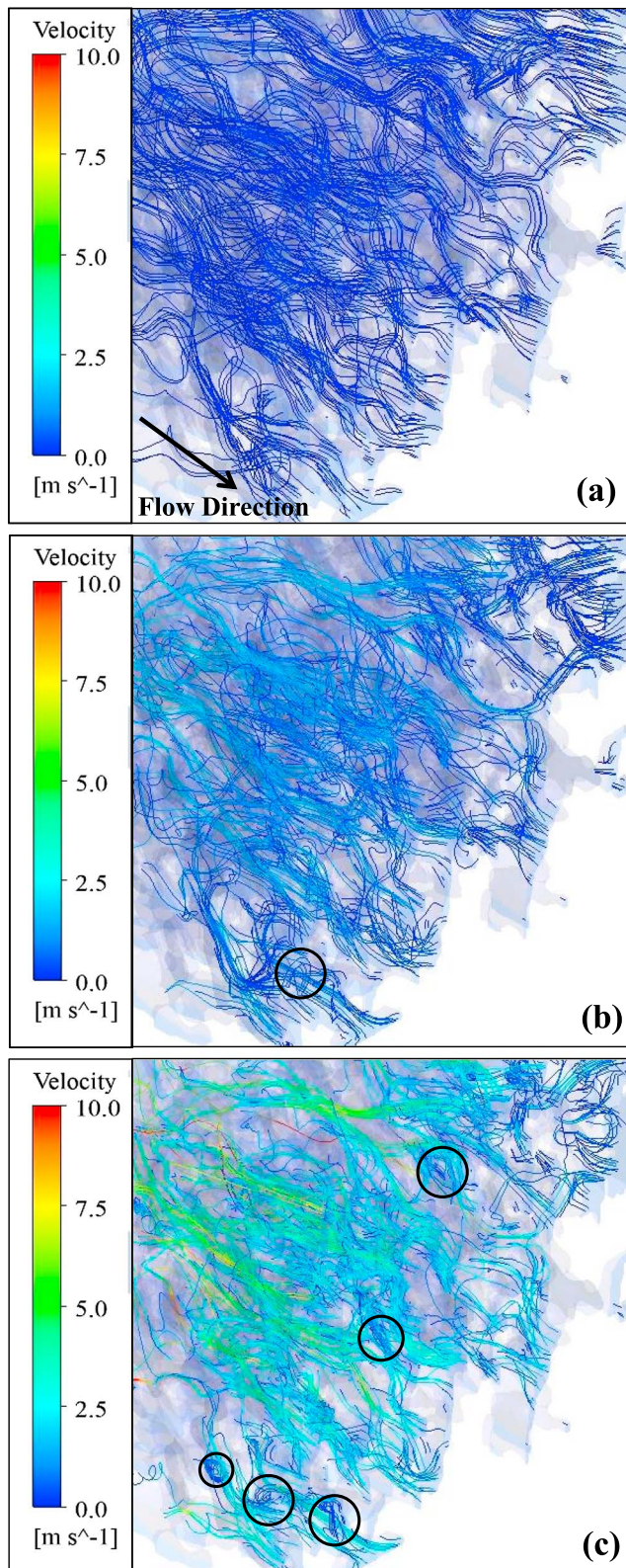


Figure 9. Plots of flow streamlines within pore space of sample S1 at selected locations during Reynolds number (a) $Re = 20$, (b) $Re = 600$, and (c) $Re = 2200$. The blue lines are streamlines, and the black circles demonstrate several eddies in Forchheimer flow regime.

dominated by viscous forces, and the exact nature of the seepage characteristics is determined by the local geometry (Dybbbs & Edwards, 1984). As shown in Figures 10b–10d, at much higher flow rates, the flow patterns in the Forchheimer regime become focused in a narrow high-velocity zone—an inertial core (Dybbbs & Edwards, 1984; Muljadi et al., 2016). Here the influence of the inertial core becomes increasingly more significant on the flow distribution and characteristics with an increase in flow rate, while the influence of pore structure decreases.

5. Discussions

5.1. The Numerical Estimation of β -Factor and its Comparison With Previous Models

5.1.1. The Numerical Estimation of β -Factor

The relation between pressure gradient and velocity in the non-Darcy flow regime is usually described by the Forchheimer equation, in which the deviation from the Darcy's law is proportional to the inertial resistance factor (β -factor) of inertial term (Newman & Yin, 2013). The non-Darcy coefficient β is considered as an intrinsic property of a porous medium and depends on the pore architecture and morphology. The β -factor is not usually measured in routine core analysis and requires a correlation to enable its prediction from other characteristic properties of the porous medium (Thauvin & Mohanty, 1998).

One method to estimate the non-Darcy coefficient β , based on simulation results, is adopted based on equation (4), and using a stepwise manner estimation method, as follows. Figure 11 shows the inverse of the apparent permeability $\frac{1}{K_{app}}$ as a function of $\frac{\rho v}{\mu}$ for samples S1, S2, and S3. Based on these results, the non-Darcy coefficient β can be calculated from the slope of the function, and the β -factors of samples S1, S2, and S3 are 4.58×10^5 , 1.81×10^5 , and $1.30 \times 10^5 \text{ m}^{-1}$, respectively.

5.1.2. Comparison of Predicted β -Factor Against Empirical Correlations

The β factor can be estimated by using an empirical Ergun equation (Ergun, 1952):

$$\beta_{Ergun} = \frac{142887}{K^{0.5}\Phi^{1.5}} \quad (11)$$

where K is the experimental permeability and Φ is the measured porosity (Table 1). The non-Darcy coefficient β_{Ergun} is $1.67 \times 10^5 \text{ m}^{-1}$ for sample S2 and $0.93 \times 10^5 \text{ m}^{-1}$ for sample S3. These agree well with our numerical estimation of the β -factors for S2 and S3 of 1.81×10^5 and $1.30 \times 10^5 \text{ m}^{-1}$, respectively.

Several empirical correlations for estimating the non-Darcy coefficient β (Ergun, 1952; Evans & Civan, 1994; Geertsma, 1974; Janicek, 1955; Jones, 1987; Li et al., 2001; Thauvin & Mohanty, 1998) are summarized in Table 5. We estimate the non-Darcy coefficient β for sample S1 by these empirical equations, where the porosity Φ and K are recovered from Table 1, with the tortuosity regressed and the results listed in Table 2. For fluid flow through a porous medium, the β values calculated by different empirical formulas vary broadly. The primary reason for this

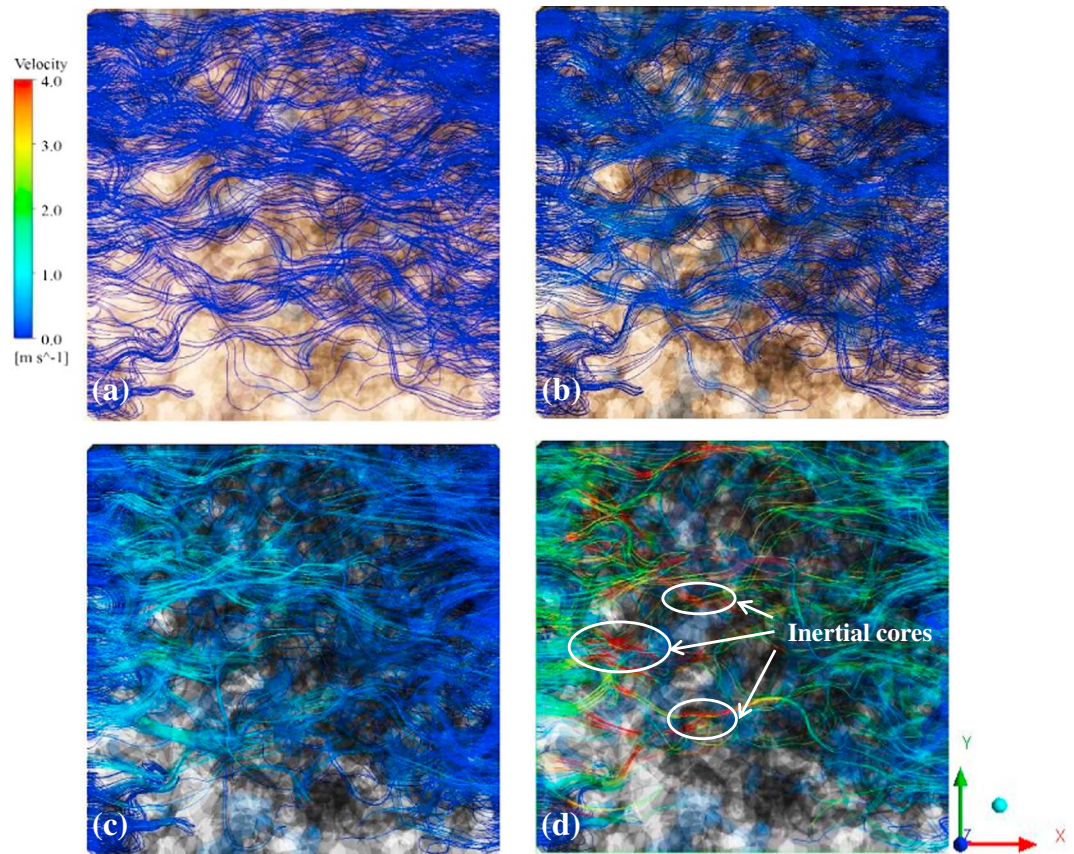


Figure 10. Plots of flow streamlines within pore space (light black) of sample S1 with the increasing Reynolds number (a) $Re=1$, (b) $Re=40$, (c) $Re=200$, and (d) $Re=900$. The streamlines are colored based on the magnitude of velocity.

difference is that some of the empirical formulae are only affected by permeability, some are more sensitive to porosity rather than permeability, and others are influenced by porosity, permeability, and tortuosity (Xu et al., 2012). Table 5 shows that the estimated β -factor of sample S1 varies from 4.00×10^4 to $1.34 \times 10^5 \text{ m}^{-1}$. The wide range of these results envelops the numerical results of $2.88 \times 10^5 \text{ m}^{-1}$ for sample S1. Thus, the numerical method proposed in this paper can provide a good prediction of the non-Darcy coefficient β for the tested artificial cores.

5.2. The Prediction of the Model of K^*-Re

The previous investigation carried out by Bolève et al. (2007) shows that the Re characterizes the influence of the inertial force in the Navier-Stokes equation. A new expression for the Re has been derived when viscous laminar flow and pore water conduction dominate. In the transition between the viscous and inertial laminar flow regimes, the reduced permeability falls as $1/(1 + Re')$ with the increase of the Re . Our research result of relationship between apparent permeability and Re was compared to their model, as shown in Figure 12. Results of Figure 12b suggest that the predicted model between the reduced permeability and Re of $k/k_0 = 1/(1 + Re')$ may lead to incorrect analysis of flow behavior when evaluating non-Darcy flow effects in porous media. As shown in Figure 12c, a new function of $k/k_0 = 1/(1 + \alpha' \times Re')$ including a parameter α' could describe well the non-Darcy flow patterns in porous media. In our opinion, there is exiting key parameters that determine the transition of flow patterns (from viscous to inertial flow regimes) in terms of apparent permeability and Re .

To further analyze the effect of those key parameters on the microscopic flow behavior in porous media, especially non-Darcy flow, a new equation (equation (6)) is formulated to predict the flow transition as a function of the apparent permeability K^* and Re based on the simulated data and analysis. For the K^*-Re model,

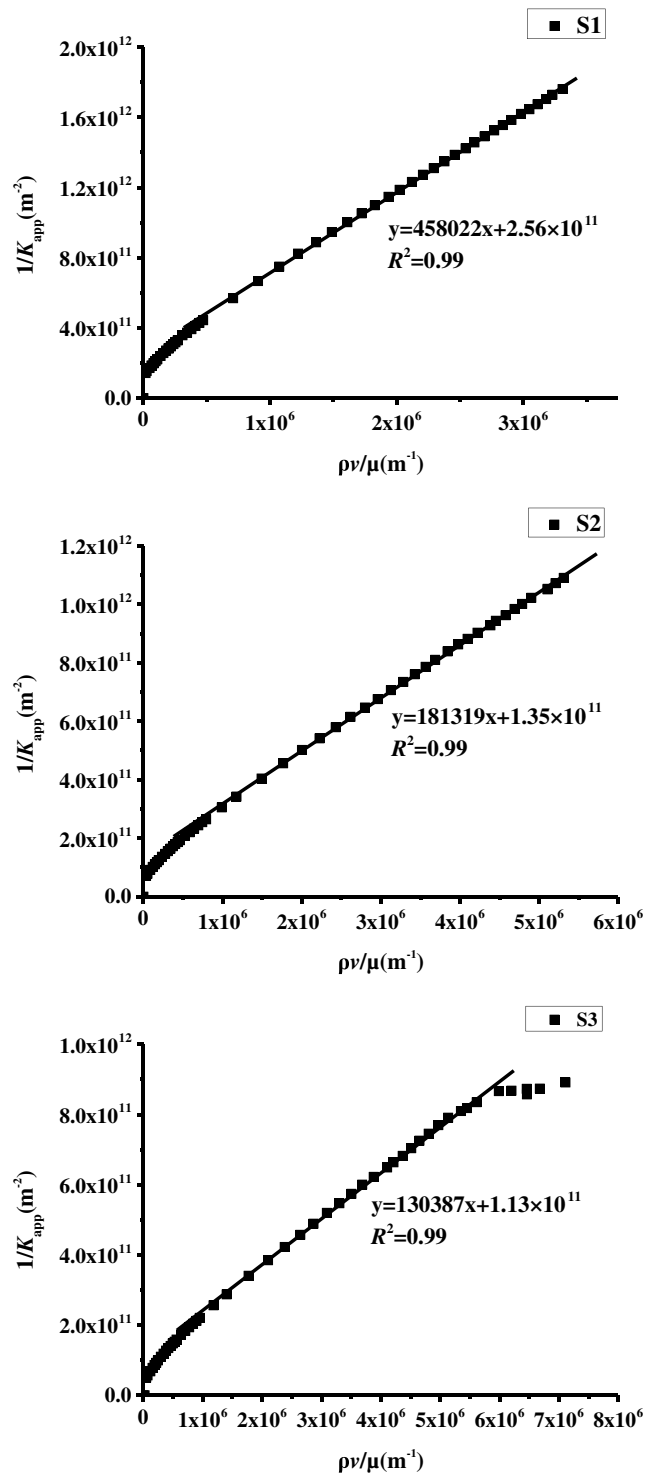


Figure 11. The curves of sample S1, S2, and S3 where $1/K_{app}$ is plotted as a function of $\rho v/\mu$ and the non-Darcy coefficient β factors are obtained from the slopes of the curves.

the empirical parameter α , the Darcy permeability K_D (flow property), the grain diameter L_0 (structure property), and the β -factor are used to quantitatively define the transition from Darcian to non-Darcian flow in a porous medium. A comparison between the predicted data from the K^*-Re model and the numerical simulated data is made in Figure 13. The results demonstrate that the predicted data for the

Table 5
The Non-Darcy Coefficient β Correlation Empirical Formulas Proposed by Different Researchers and the Calculate Values of β Factors

Formula no.	Correlation	Units of β and K_D	Values of $\beta \times 10^5 \text{ m}^{-1}$
			S1
1	$\beta = \frac{4.24 \times 10^6}{\sqrt{K_D \Phi^{1.5}}}$ (Evans & Civan, 1994)	m^{-1}, mD	2.70
2	$\beta = \frac{5.5 \times 10^9}{K_D^{1.25} \Phi^{0.75}}$ (Evans & Civan, 1994)	m^{-1}, mD	3.08
3	$\beta = \frac{1.15 \times 10^9}{K_D \Phi}$ (Li et al., 2001)	m^{-1}, mD	6.73
4	$\beta = \frac{2.018 \times 10^{11}}{K_D^{1.35}}$ (Jones, 1987)	m^{-1}, mD	4.39
5	$\beta = \frac{1.82 \times 10^8}{K_D^{1.25} \Phi^{0.75}}$ (Janicek, 1955)	$\text{cm}^{-1}, \text{mD}$	10.20
6	$\beta = \frac{0.005}{K_D^{0.5} \Phi^{2.5}}$ (Geertsma, 1974)	$\text{cm}^{-1}, \text{cm}^2$	4.83
7	$\beta = \frac{15500 r^{3.35} \Phi^{0.29}}{K_D^{0.98}}$ (Thauvin & Mohanty, 1998)	cm^{-1}, D	6.99

core sample, based on the empirical parameter α , the Darcy permeability K_D , grain diameter L_0 , and the non-Darcy coefficient β , are in excellent agreement with the trend of flow transition in Forchheimer regimes. The magnitudes of the empirical coefficient α for different core samples are close to 2, in which α values of samples S1, S2, and S3 are specifically 2.31, 2.00, and 2.22, respectively. This finding shows that the K^2 - Re model determined by the non-Darcy coefficient β and other properties provides a rational way to describe

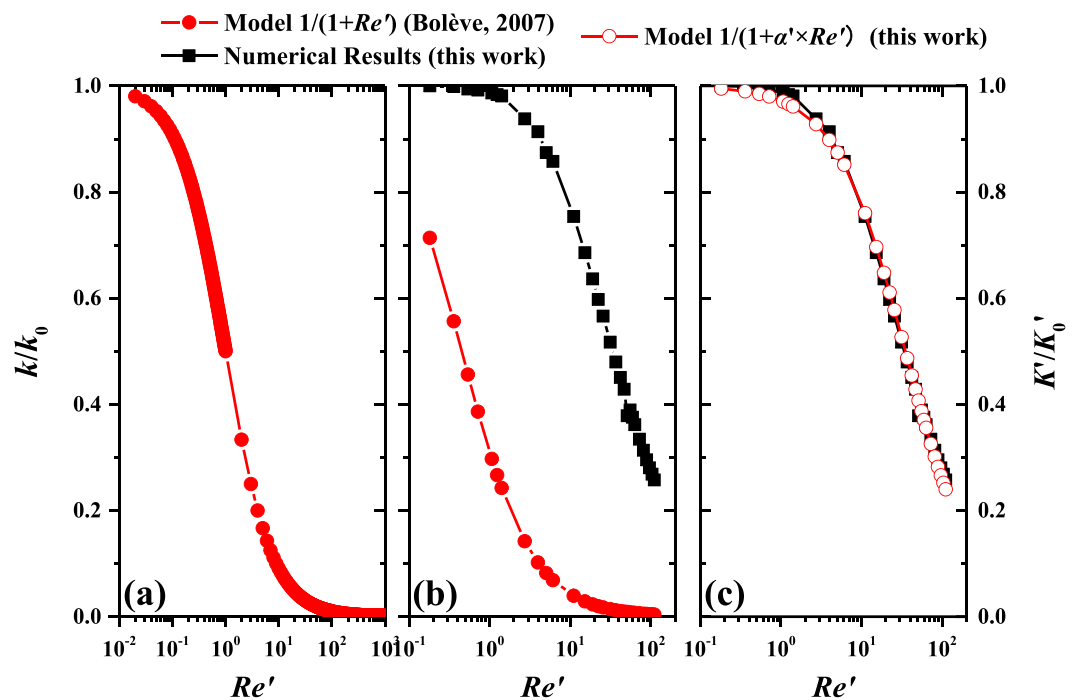


Figure 12. Comparison of the results of the relationship between K'/K_0' (where K' is apparent permeability of non-Darcy flow obtained by the numerical simulation and K_0' represents the permeability in Darcy flow state, which is approximate equal to the experimental permeability) and Reynolds number (where $Re' = \rho vr/\mu$ and r is the pore radius) to the prediction model (Bolève et al., 2007) of $k/k_0 = 1/(1 + Re')$. where the parameter $\alpha = 0.0064$ for the model $k/k_0 = 1/(1 + \alpha' \times Re')$.

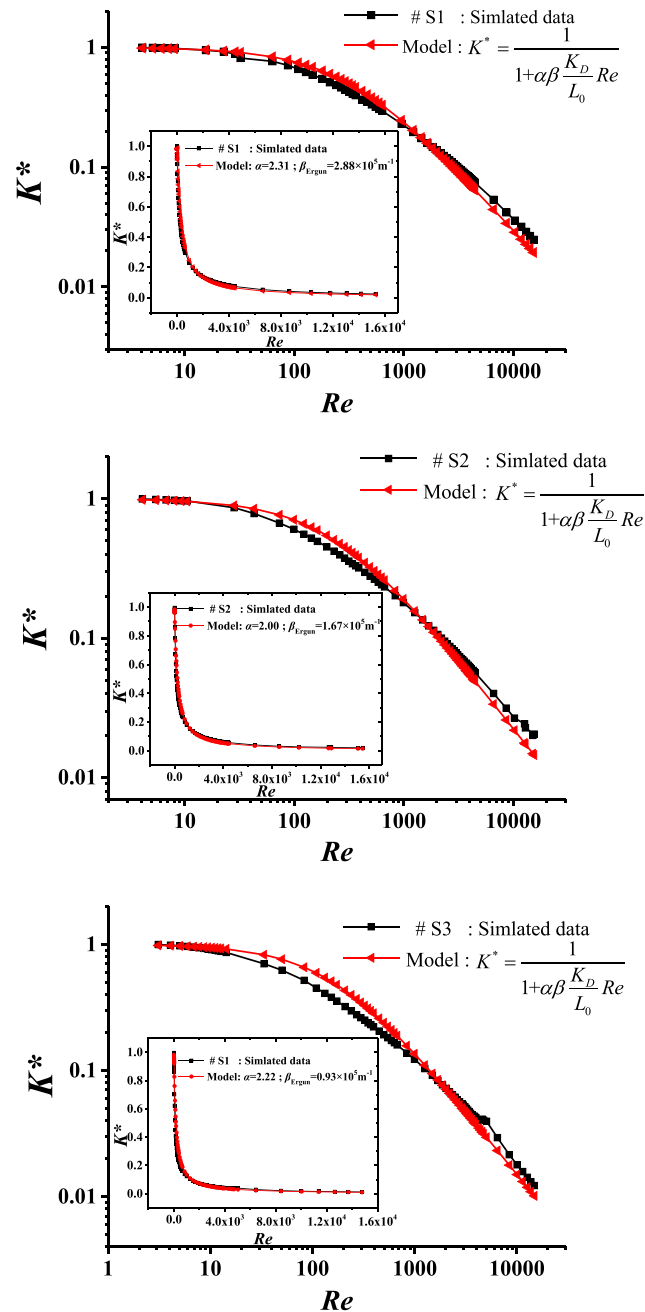


Figure 13. The comparison between the data computed for different model parameters and the simulated data in artificial cores, where the β_{Ergun} factors are calculated by Ergun equation and parameter α is the empirical coefficient to decrease the inertial effects in non-Darcy flow regimes.

the transition from Darcy to Forchheimer flow. Moreover, the Darcy and Forchheimer equations, defined as the ratio of inertial forces to viscous forces and Re , are found more adequate for analyzing microscopic non-Darcy flow behaviors in porous media.

6. Summary and Conclusion

In this study, we propose a new pore-scale approach to investigate single-phase flow and its transition to the non-Darcy flow regime in reconstructed 3-D porous media. The 3-D pore-scale model is recovered from a

synthetic core. This is completed by utilizing CT images to represent the actual pore geometry of the tested cores. This digital rock physics methodology is adopted to quantitatively reconstruct the pore architecture and characteristics of the cores and furthermore to define transport properties. Based on the numerical simulation results for single phase fluid flows, the following conclusions are made.

1. It is demonstrated that the smaller the permeability, the greater the critical pressure gradient for the transition to non-Darcy flow and the easier the emergence of nonlinear seepage phenomena. The emergence of nonlinear seepage phenomena coincides with a decrease of porosity and an increase of tortuosity in artificial cores. The relationship between permeability and porosity from different methods shows a power law correlation.
2. The structural heterogeneity and anisotropy of the pore systems exert a significant influence on fluid flow and transport through the 3-D pore network. The distribution of fluid flow fields within the pore space are irregular, and the simulated permeability of different artificial core samples varies by a factor of 2–5 depending on the fluid flow directions.
3. With the growth in flow velocity, eddies emerge within the pore voids and reduce the effective dimension of the void—effectively constricting the flow. This reduction is physically reflected in the reduction in the apparent permeability. The simulation results demonstrate that the larger the porosity of the artificial core samples, the more obvious this nonlinear phenomenon of seepage within the pore space. The presence of an inertial core becomes more and more significant on the flow characteristics with an increase in the flow velocity, while the influence of pore structure decreases.
4. Based on the pore-scale simulation results for the non-Darcy flow regimes, a method is applied to estimate the non-Darcy coefficient β , which can provide a good prediction for the tested artificial cores. A new equation is formulated to predict the transition of flow patterns as a function of the apparent permeability K^* and Re . The predicted results, based on the β_{Ergun} factors, are in excellent agreement with the simulated trend of flow transition in the Forchheimer regimes. For the K^*-Re model, the model is determined by the non-Darcy coefficient β and provides a method to describe and to index the transition from Darcy to Forchheimer flow.

Acknowledgments

The results presented in this article rely on the data collected at the State Key Laboratory of Coal Resources and Safe Mining, China University of Mining and Technology Beijing. Data are available to external users upon request provided that proper acknowledgement is applied in subsequent reporting. The research is financially supported by the National Key Research and Development Program of China (2016YFC0600708 and 2016YFC0801401), Yue Qi Distinguished Scholar Project of China University of Mining and Technology (Beijing), and Fundamental Research Funds for the Central Universities. The authors specially thank Jiaojiao Li, Shanbin Xue, and Quan Gan for their suggestions and aid in both conducting the simulation and analysis of the results. The editor Andre Revil and anonymous reviewers are appreciated for their comments, which improved an earlier version of this paper.

References

- Ahuja, L. R. (1989). Evaluation of spatial distribution of hydraulic conductivity using effective porosity data. *Soil Science*, 148(6), 404–411. <https://doi.org/10.1097/00010694-198912000-00002>
- Arns, C. H., & Knackstedt, M. A. (2004). Virtual permeametry on microtomographic images. *Journal of Petroleum Science & Engineering*, 45(1-2), 41–46. <https://doi.org/10.1016/j.petrol.2004.05.001>
- Bachu, S. (2000). Sequestration of CO₂ in geological media: Criteria and approach for site selection in response to climate change. *Energy Conversion and Management*, 41(9), 953–970. [https://doi.org/10.1016/S0196-8904\(99\)00149-1](https://doi.org/10.1016/S0196-8904(99)00149-1)
- Bear, J. (1972). *Dynamics of Fluids in Porous Media*. Mineola, New York: Dover.
- Bird, M. B., Butler, S. L., Hawkes, C. D., & Kotzer, T. (2014). Numerical modeling of fluid and electrical currents through geometries based on synchrotron X-ray tomographic images of reservoir rocks using Avizo and COMSOL. *Computers & Geosciences*, 73(C), 6–16. <https://doi.org/10.1016/j.cageo.2014.08.009>
- Bolève, A., Crespy, A., Revil, A., Janod, F., & Mattiuzzo, J. L. (2007). Streaming potentials of granular media: Influence of the Dukhin and Reynolds numbers. *Journal of Geophysical Research*, 112, B08204. <https://doi.org/10.1029/2006JB004673>
- Boone, M. A., Kock, T. D., Bultreys, T., Schutter, G. D., Vontobel, P., Hoorebeke, L. V., & Cnudde, V. (2014). 3D mapping of water in oolitic limestone at atmospheric and vacuum saturation using X-ray micro-CT differential imaging. *Materials Characterization*, 97, 150–160. <https://doi.org/10.1016/j.matchar.2014.09.010>
- Chaudhary, K., Cardenas, M. B., Deng, W., & Bennett, P. C. (2011). The role of eddies inside pores in the transition from Darcy to Forchheimer flows. *Geophysical Research Letters*, 38, L24405. <https://doi.org/10.1029/2011GL050214>
- Chukwudozie, C. P., Tyagi, M., Sears, S. O., & White, C. D. (2012). Prediction of non-Darcy coefficients for inertial flows through the Castlegate sandstone using image-based modeling. *Transport in Porous Media*, 95(3), 563–580. <https://doi.org/10.1007/s11242-012-0062-5>
- Comiti, J., Sabiri, N. E., & Montillet, A. (2000). Experimental characterization of flow regimes in various porous media—III: Limit of Darcy's or creeping flow regime for Newtonian and purely viscous non-Newtonian fluids. *Chemical Engineering Science*, 55(15), 3057–3061. [https://doi.org/10.1016/S0009-2509\(99\)00556-4](https://doi.org/10.1016/S0009-2509(99)00556-4)
- Darcy, H. (2012). *Les Fontaines Publiques de la Ville de Dijon*. Paris: Dalmont.
- Dong, H., Touati, M., & Blunt, M. (2007). Pore network modeling: Analysis of pore size distribution of Arabian core samples, in SPE middle east oil and gas show and conference, Kingdom of Bahrain. Society of Petroleum Engineers. <https://doi.org/10.2118/105156-MS>
- Dunsmuir, J. H., Ferguson, S. R., D'Amico, K. L., & Stokes, J. P. (1991). X-ray microtomography: A new tool for the characterization of porous media. In *SPE Technical Conference and Exhibition*. Dallas, TX.
- Dybbas, A., & Edwards, R. V. (1984). *A new look at porous media fluid mechanics—Darcy to turbulent* (pp. 199–256). Netherlands: Springer. https://doi.org/10.1007/978-94-009-6175-3_4
- Ergun, S. (1952). Fluid flow through packed columns. *Chemical Engineering Progress*, 48(2), 89–94.
- Evans, R. D., & Civan, F. (1994). Characterization of non-Darcy multiphase flow in petroleum bearing formation. Final report Rep., U.S. DOE contract no. DE-AC22-90BC14659, School of Petroleum and Geological Engineering, University of Oklahoma.
- Forchheimer, P. H. (1901). Wasserbewegung Durch Boden. *Zeitschrift Vereines Deutscher Ingenieure*, 45, 1782–1788.

- Fourar, M., Radilla, G., Lenormand, R., & Moyne, C. (2004). On the non-linear behavior of a laminar single-phase flow through two and three-dimensional porous media. *Advances in Water Resources*, 27(6), 669–677. <https://doi.org/10.1016/j.advwatres.2004.02.021>
- Geertsma, J. (1974). Estimating the coefficient of inertial resistance in fluid flow through porous media. *Society of Petroleum Engineers Journal*, 14(05), 445–450. <https://doi.org/10.2118/4706-PA>
- Gruber, I., Zinovik, I., Holzer, L., Flisch, A., & Poulikakos, L. D. (2012). A computational study of the effect of structural anisotropy of porous asphalt on hydraulic conductivity. *Construction and Building Materials*, 36, 66–77. <https://doi.org/10.1016/j.conbuildmat.2012.04.094>
- Janicek, J. D. (1955). Applications of unsteady state gas flow calculations, in U. Michigan Research Conference, edited, June 1955.
- Jones, S. C. (1987). Using the inertial coefficient, B, to characterize heterogeneity in reservoir rock. In *SPE Annual Technical Conference and Exhibition*, Edited, Dallas, TX.
- Keller, L. M., Holzer, L., Wepf, R., Gasser, P., Münch, B., & Marschall, P. (2011). On the application of focused ion beam nanotomography in characterizing the 3D pore space geometry of Opalinus clay. *Physics and Chemistry of the Earth*, 36(17-18), 1539–1544. <https://doi.org/10.1016/j.pce.2011.07.010>
- Korvin, G. (2016). Permeability from microscopy: Review of a dream. *Arabian Journal for Science and Engineering*, 41(6), 2045–2065.
- Leahy-Dios, A., Das, M., Agarwal, A., & Kaminsky, R. D. (2011). *Modeling of transport phenomena and multicomponent sorption for shale gas and coalbed methane in an unstructured grid simulator*. Paper presented at SPE Annual Technical Conference, Denver, CO.
- Li, D., Svec, R. K., Engler, T. W., & Grigg, R. B. (2001). Modeling and simulation of the wafer non-Darcy flow experiments. In *Spe Western Regional Meeting* (SPE-68822-MS). Bakersfield, CA: Society of Petroleum Engineers. <https://doi.org/10.2118/68822-MS>
- Liu, X. J., Zhu, H. L., & Liang, L. X. (2014). Digital rock physics of sandstone based on micro-CT technology. *Chinese Journal of Geophysics*, 57(4), 1133–1140.
- Lorensen, W. E., & Cline, H. E. (1987). Marching cubes: A high resolution 3D surface construction algorithm. In *Computer Graphics and Interactive Techniques* (pp. 163–169). New York.
- Muljadi, B. P., Blunt, M. J., Raeni, A. Q., & Bijeljic, B. (2016). The impact of porous media heterogeneity on non-Darcy flow behaviour from pore-scale simulation. *Advances in Water Resources*, 95, 329–340. <https://doi.org/10.1016/j.advwatres.2015.05.019>
- Newman, M. S., & Yin, X. (2013). Lattice Boltzmann simulation of non-Darcy flow in stochastically generated 2D porous media geometries. *SPE Journal*, 18(01), 12–26. <https://doi.org/10.2118/146689-PA>
- Ni, X., Miao, J., Lv, R., & Lin, X. (2017). Quantitative 3D spatial characterization and flow simulation of coal macropores based on μ CT technology. *Fuel*, 200, 199–207. <https://doi.org/10.1016/j.fuel.2017.03.068>
- Otsu, N. (2007). A threshold selection method from gray-level histograms. *IEEE Transactions on Systems, Man, and Cybernetics*, 9(1), 62–66.
- Ovaysi, S., & Piri, M. (2010). Direct pore-level modeling of incompressible fluid flow in porous media. *Journal of Computational Physics*, 229(19), 7456–7476. <https://doi.org/10.1016/j.jcp.2010.06.028>
- Pi, Y. (2010). Type and application of special artificial cores. *Science Technology & Engineering*, 10(31), 7724–7727.
- Schaap, M. G., & Lebron, I. (2001). Using microscope observations of thin sections to estimate soil permeability with the Kozeny–Carman equation. *Journal of Hydrology*, 251(3–4), 186–201. [https://doi.org/10.1016/S0022-1694\(01\)00468-1](https://doi.org/10.1016/S0022-1694(01)00468-1)
- Song, R., Liu, J., & Cui, M. (2017). A new method to reconstruct structured mesh model from micro-computed tomography images of porous media and its application. *International Journal of Heat and Mass Transfer*, 109, 705–715. <https://doi.org/10.1016/j.jijheatmasstransfer.2017.02.053>
- Spanne, P., Thovert, J. F., Jacquin, C. J., Lindquist, W. B., Jones, K. W., & Adler, P. M. (1994). Synchrotron computed microtomography of porous media: Topology and transports. *Physical Review Letters*, 73(14), 2001–2004. <https://doi.org/10.1103/PhysRevLett.73.2001>
- Sukop, M. C., Huang, H., Alvarez, P. F., Variano, E. A., & Cunningham, K. J. (2013). Evaluation of permeability and non-Darcy flow in vuggy macroporous limestone aquifer samples with Lattice Boltzmann methods. *Water Resources Research*, 49, 216–230. <https://doi.org/10.1029/2011WR011788>
- Thauvin, F., & Mohanty, K. K. (1998). Network modeling of non-Darcy flow through porous media. *Transport in Porous Media*, 31(1), 19–37. <https://doi.org/10.1023/A:1006558926606>
- Thermo Fisher Scientific & FEI (2013). Avizo User's Guide. Retrieved from <http://www.vsg3d.com/sites/default/files/AvizoRefGuide.pdf>
- Wang, G., Yang, X., Zhang, X., Li, W., & Shi, L. (2016). Numerical simulation of gas flow in pores and fissures of coal based on segmentation of DTM threshold. *Chinese Journal of Rock Mechanics and Engineering*, 45(1), 119–129.
- Xu, H., Tang, D., Zhao, J., & Li, S. (2015). A precise measurement method for shale porosity with low-field nuclear magnetic resonance: A case study of the Carboniferous–Permian strata in the Linxing area, eastern Ordos Basin, China. *Fuel*, 143, 47–54. <https://doi.org/10.1016/j.fuel.2014.11.034>
- Xu, K., Lei, X., Meng, Q., & Zhou, X. (2012). Study of inertial coefficient of non-Darcy seepage flow. *Chinese Journal of Rock Mechanics and Engineering*, 31(1), 164–170.
- Yan, Z., Geiger, S., Sorbie, K., & Förster, M. (2010). Efficient flow and transport simulations in reconstructed 3D pore geometries. *Advances in Water Resources*, 33(12), 1508–1516.
- Yang, F., Ning, Z., Hu, C., Wang, B., Peng, K., & Liu, H. (2013). Characterization of microscopic pore structures in shale reservoirs. *Acta Petroli Sinica*, 34(2), 301–311.
- Yao, Y., Liu, D., Cai, Y., & Li, J. (2010). Advanced characterization of pores and fractures in coals by nuclear magnetic resonance and X-ray computed tomography. *Science China Earth Sciences*, 53(6), 854–862. <https://doi.org/10.1007/s11430-010-0057-4>
- Zhang, L., Kang, Q. J., Yao, J., Gao, Y., Sun, Z. X., Liu, H. H., & Valocchi, A. J. (2015). Pore scale simulation of liquid and gas two-phase flow based on digital core technology. *Science China Earth Sciences*, 58(8), 1375–1384.
- Zhang, P., Liu, X., Wang, Y., & Sun, X. (2014). Research progress in shale nanopores. *Advances in Earth Science*, 29(11), 1242–1249.
- Zhao, Y., Zhu, G., Dong, Y., Danesh, N. N., Chen, Z., Zhang, T., et al. (2017). Comparison of low-field NMR and microfocus X-ray computed tomography in fractal characterization of pores in artificial cores. *Fuel*, 210, 217–226. <https://doi.org/10.1016/j.fuel.2017.08.068>